CHAPTER 3

Study of structural, compositional and optical properties of MoS_2, WS_2 and ternary compound MoW-disulfide NPs

3 Study of structural, compositional and optical properties of MoS_2, WS_2 and ternary compound MoW-disulfide NPs

The detailed analysis of various characterization results of ternary compound disulfides of Mo and W have been discussed in this chapter. Differences in optical properties of such TMD NPs and differences in their structure have been investigated and reported in this chapter. The structural and optical properties of our as-synthesized MoS_2 and WS_2 NPs and ternary disulfides of Mo and W, namely MoW-disulfide1 and MoW-disulfide2 were reported and compared the findings with existing literature. The chapter is mainly divided into four sections. Section 3.1 deals in the structural and optical properties of MoS_2 NPs, section 3.2 deals in the structural and optical properties of WS_2 NPs, section 3.3 deals in the structural and optical properties of the ternary compound MoW-disulfide NPs and section 3.4 deals in the photoluminescent behavior of the as-synthesized NPs. Experimental observations reveal that the structural behavior remains intact in the as-synthesized ternary TMD NPs like that of MoS_2 and WS_2 NPs, however, there is slight modification due to the formation of new bonds in the ternary compounds. There are some interesting changes in the optical properties of the ternary compounds as well which leads to enhancement in the luminescence and photocatalytic behavior of the as-synthesized compound disulfides. The structural and optical characterization of the as-synthesized MoS_2, WS_2 and compound MoW-disulfide NPs are discussed in the following sections.

3.1 Structural and optical properties of MoS_2 NPs

3.1.1 Structural characterizations of MoS_2 NPs

The morphology of the as-synthesized MoS_2 NPs were studied by using different analytic techniques such as XRD, TEM, SEM, Raman spectroscopy etc. Compositional analysis was performed by using EDS and elemental mapping was obtained with SEM.

Figure 3.1 is the XRD pattern of MoS_2 NPs obtained from X-ray Diffractometer (make: RIGAKU MINIFLEX) with Cu-Kα radiation (λ= 1.5405 Å) in the 2θ range from 10º to 70º. For the MoS_2 sample XRD peaks at 2θ equal to 14.24°, 28.36°, 33.01°, 35.83°, 42.98°, 58.71°, 58.90° correspond to the Millar crystal planes (002), (004), (100), (102), (006), (110), (008) respectively when compared with JCPDS software having file No. 75-1539 (PCPDFWIN v.2.02). These Millar planes correspond to the system having hexagonal

symmetry (SG:$p6_3/mmc$) in MoS_2 lattice. The broadening nature of the XRD peaks is a sign of the smaller crystallite size of the MoS_2 NPs. Also, the XRD pattern reveals that the material is polycrystalline in nature. The crystallite size (L) is calculated using Debye-Scherrer formula 3.1 [1].

$$L = \frac{C_2 \lambda}{\beta \cos\theta} \qquad (3.1)$$

where λ, β and θ are the wavelength of X-ray, full width at half maximum (F.W.H.M.) (in radian) of XRD-peak and corresponding Bragg's angle of diffraction peak respectively and C_2 is a constant depending on the assumption made in the theory (in most cases always close to unity and taken to be 0.91). Using relation 3.1 the average crystallite size of the synthesized MoS_2 NPs was calculated to be approximately 11.07 nm.

The simulated powdered XRD (PXRD) pattern for MoS_2 sample in comparison with the experimentally obtained XRD pattern was also plotted in figure 3.1(b). The simulation was done by using the standard software VESTA 3(Visualization for Electronic and STructural Analysis, version 3) [2]. It is obvious that experimentally synthesized materials have impurities and show deviations, but our experimental XRD plots for MoS_2 shows similarity with the simulated one to a great extent as shown in figure 3.1(b).

TEM analysis was performed to obtain the structural information. The TEM micrograph in figure 3.2(a) shows different crystal planes present in the as-prepared MoS_2 sample. From the crystal planes observed in TEM micrograph, the interplanar spacing 0.63nm and 0.31nm, shown in figure 3.2(a), were determined. These corresponded to the Millar plane (002) and (004) respectively in the MoS_2 crystal. The selected area electron diffraction (SAED) pattern, shown in figure 3.2(c), which was also obtained from TEM confirmed that the as-synthesized MoS_2 NPs were polycrystalline in nature. Figure 3.2(b) shows different grains of MoS_2 NPs.

SEM image having 10,000x magnification of the as-prepared MoS_2 NPs was also obtained. The SEM image is shown in figure 3.3(a). From the SEM micrograph in figure 3.3(a) it was observed that the average particle size for MoS_2 was 62.47nm. The particle size distribution histogram of the as-synthesized materials was evaluated from SEM micrographs and is shown in figure 3.3(b). However, being NPs, due to the high surface

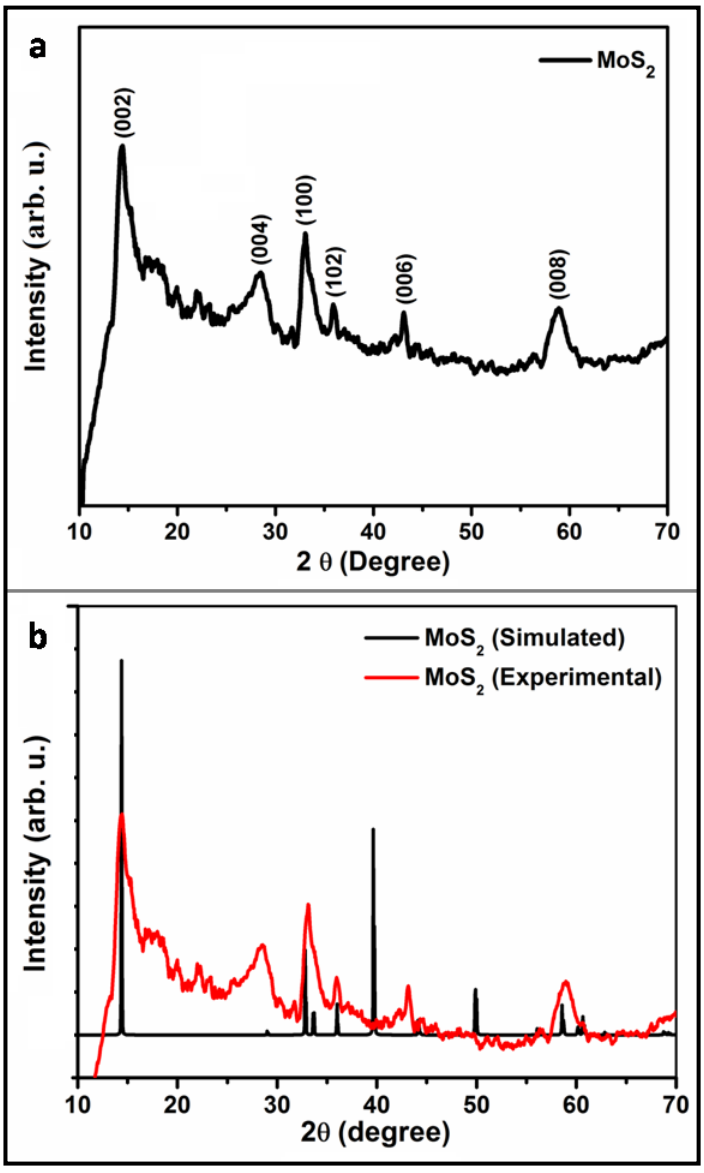

Figure 3.1 (a) XRD spectrum of MoS_2 NPs (experimental) and (b) Comparison of XRD of MoS_2 with simulated PXRD of MoS_2.

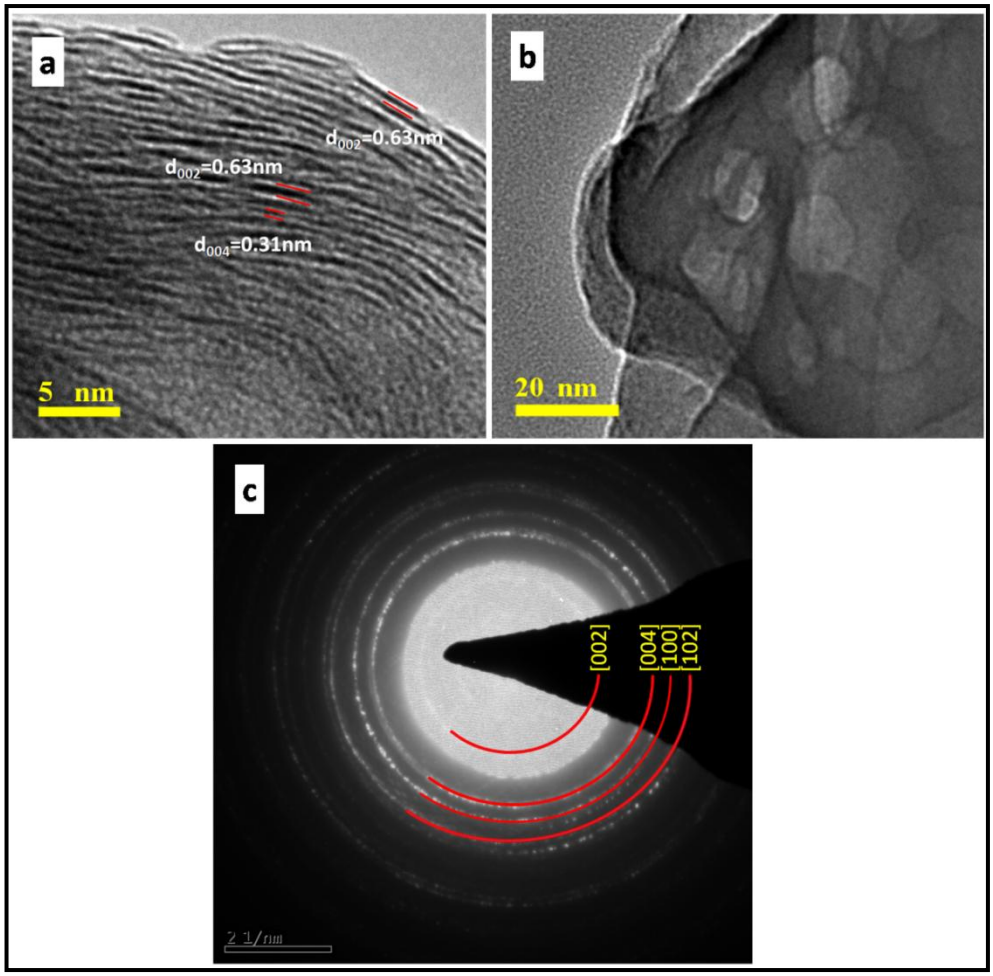

Figure 3.2 TEM image showing (a) different crystal planes, (b) a bunch of grains and (c) SAED pattern in MoS_2 NPs sample.

energy they got agglomerated and therefore, larger particles having nonuniform size distribution are also visible from the micrograph [3, 4].

In order to ascertain the composition of the material, we obtained the EDX spectrum of the MoS_2 NP sample. From the EDX spectrum analysis, given in figure 3.3(c), we conclude that the material is mainly composed of Mo and S, S being most abundant. The percentage composition of the MoS_2 NP sample is given in table 3.1. Both XRD spectra and EDX spectra revealed the formation of MoS_2. In the EDX spectrum, a characteristic peak near 2.31keV confirmed the presence of sulfur and near 2.39keV revealed the presence of Molybdenum in the respective sample [5]. Also, the abundance of specific elements and chemical composition of the as-synthesized MoS_2 NPs were envisioned in the elemental maps or spot chemical analysis using EDS given in figure 3.4.

Table 3.1 Percentage composition of MoS_2 from EDX spectrum.

Element	Weight %	Atomic %
S K	43.57	69.79
Mo L	56.43	30.21
Total	100.00	

Raman spectroscopy was also employed to study the vibrational mode of MoS_2 NP sample. We obtained Raman spectrum of the as-synthesized MoS_2 sample as it is the characteristic tool which provides a fingerprint by which the material can be identified. The Raman spectrum of the as-prepared sample was obtained with laser excitation wavelength of 488nm (2.54eV) as shown in figure 3.5.

The Raman spectrum here is given as a plot of the intensity of Raman scattered radiation as a function of its Raman shift (in units of wavenumber, cm^{-1}). The characteristic peaks 384.95cm^{-1} and 406.12cm^{-1} in the Raman spectrum of MoS_2 sample (figure 3.5(a)) revealed the Raman active vibration modes E^1_{2g} and A_{1g} (figure 3.5(b)) in MoS_2 [6-8]. There is a shift in the position of E^1_{2g} and A_{1g} mode from the bulk material at 383cm^{-1} (E^1_{2g}) and 408cm^{-1}(A_{1g}) which is due to the low dimensional effect in the NPs. The blue-shift in E^1_{2g} mode is due to the short-range coulombic interlayer interaction which changes the atomic vibration and the red-shift in A_{1g} mode is due to the smaller Van der Waals force which aids atomic vibration resulting in smaller force constant [7, 8]. Resonance

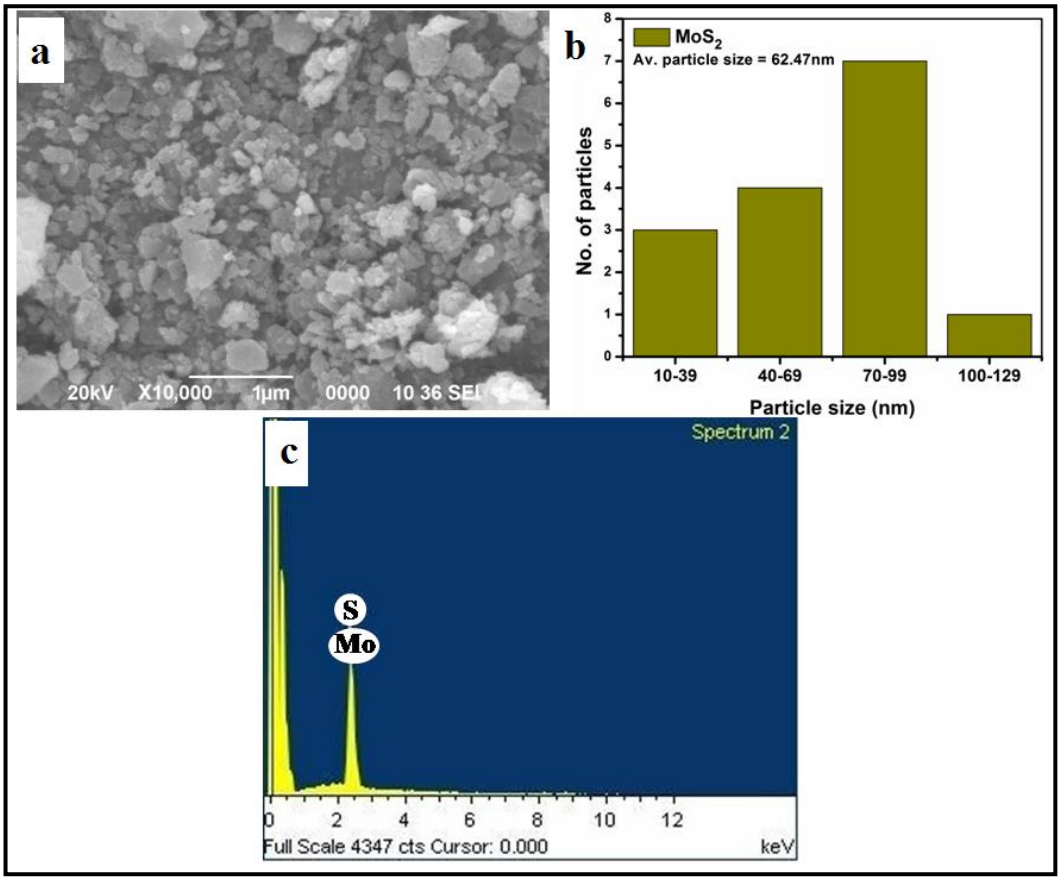

Figure 3.3 (a) SEM image, (b) particle size distribution histogram and (c) EDX spectrum of MoS_2 NPs sample. The noise peak observed below 0.5keV is not taken into consideration.

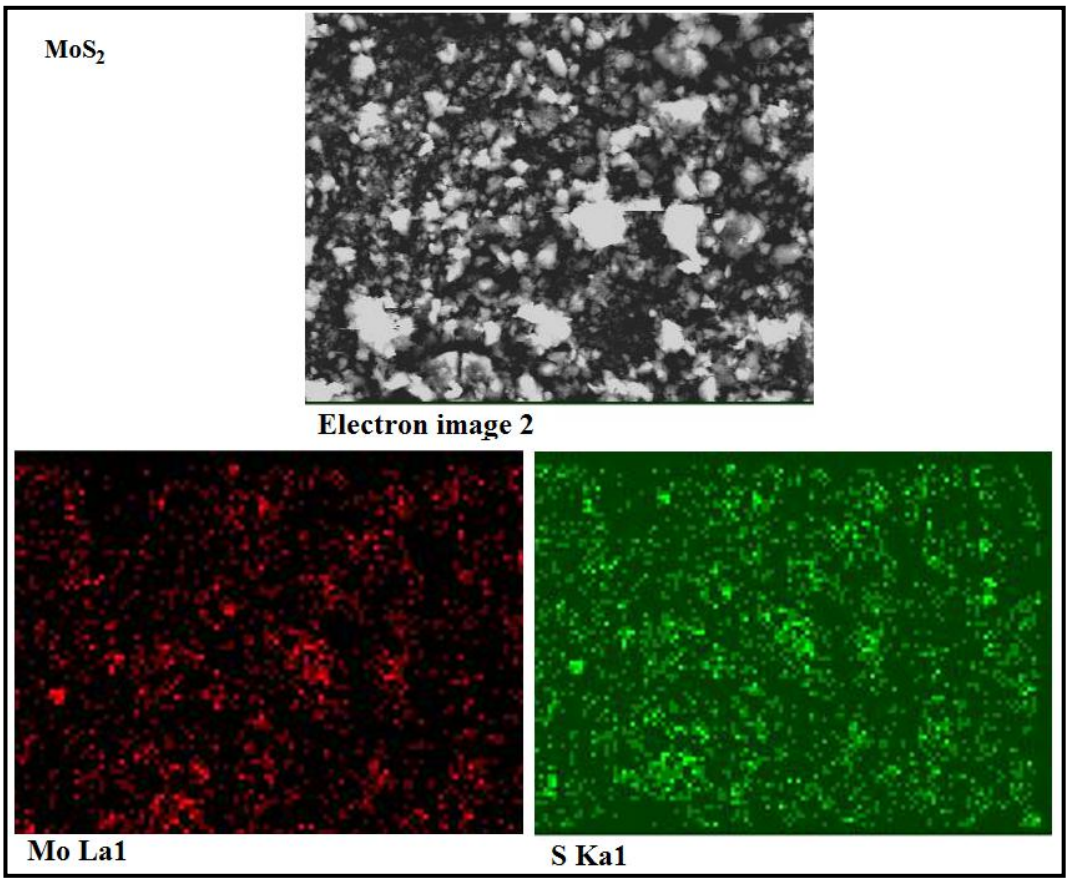

Figure 3.4 EDX spot Elemental mapping of MoS_2 NPs. The Bright spots represent the presence of respective elements in the image of Mo and S mapping.

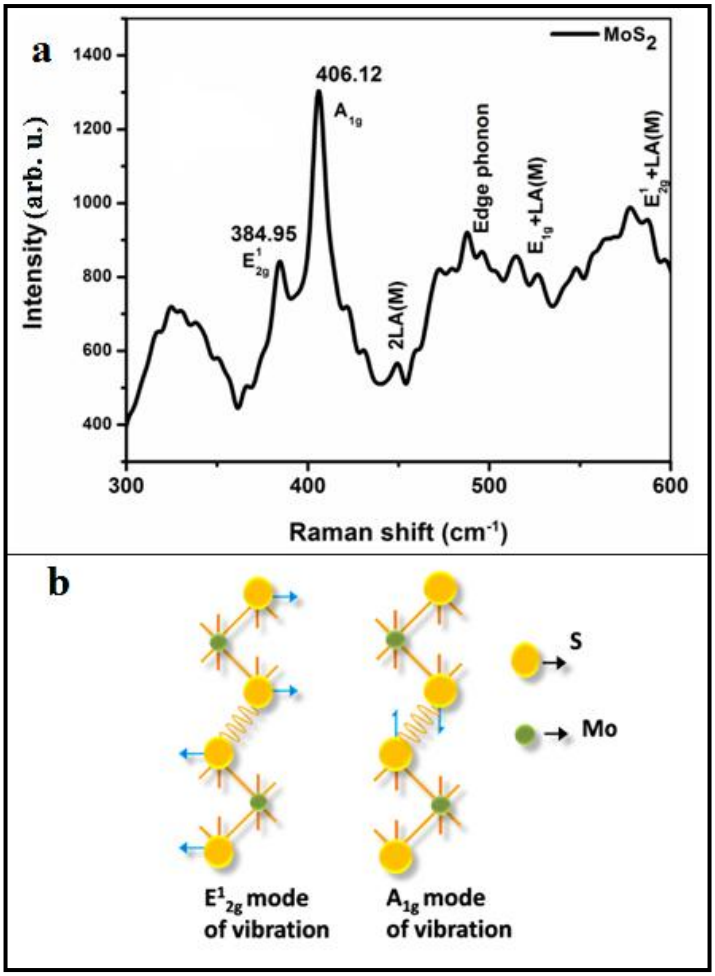

Figure 3.5 (a) Raman spectrum of MoS_2 NPs sample showing characteristics modes of vibration, (b) schematic to visualize prominent E^1_{2g} and A_{1g} modes of vibration in MoS_2.

Raman peaks were also observed at 450cm^{-1} (2LA(M)), 496 cm^{-1} (Edge phonon), 526 cm^{-1} (E_{1g} (M) + LA(M)) and 597cm^{-1} (E^1_{2g} (M)+LA(M)) because of the comparable value of excitation energy with the BG energy of the as-synthesized MoS_2 NPs [6].

Since Raman spectroscopy also detects phonon activity, the phonon lifetimes in the sample were also calculated using the energy-time uncertainty relation 3.2 [1]

$$1/\tau = \Delta E/h = \pi c \Gamma/2 \tag{3.2}$$

where ΔE is the uncertainty in energy, h is the Planck's constant, c is the speed of light in vacuum and Γ is the FWHM of the Raman peaks in cm^{-1}. The phonon lifetime corresponding to the Raman active modes E^1_{2g} and A_{1g} obtained from Raman spectra for the as-synthesized MoS_2 NPs samples were found to be in the range of picoseconds (tabulated in table 3.2). The large phonon lifetime indicates that the samples have more defect states that may trap the phonon for a longer time [9].

Table 3.2 Determination of phonon lifetime in MoS_2 NPs sample from the Raman spectrum.

Peak position (cm^{-1})	**Phonon Lifetime (ps)**
384.95	3.39
406.15	2.78

Thus analyzing all the structural characterizations using XRD, SEM, TEM, EDX, Elemental mapping and Raman spectrum we conclude that the formation of MoS_2 NPs is confirmed. Also, it was observed that the average size of the NPs was 62.47nm having average crystallite size 11.07nm.

3.1.2 Optical characterizations of MoS_2 NPs

UV-vis spectrum and PL spectrum was analyzed and the optical BG value of the synthesized material was obtained using KM plot [10, 11]. The UV-Vis spectrum (inset in figure 3.6) reveals that there is good absorption of light in the visible region (500nm to 700nm) as well as in the UV region (250nm to 400 nm) for the as-synthesized MoS_2 NPs.

The presence of more than one edge in the spectrum also indicates different dimension or phases of the same material. For the MoS_2 NP sample, near 660nm and 610nm two absorption peaks are observed, which are due to 'A' and 'B' excitonic transitions as shown in figure 3.7 [12]. The lower energy peak is due to the transition from the upper level of the spin-split valence band (VB) to the conduction band (CB). Higher energy peak for the 'B' exciton is due to the transition from the lower spin-split level of VB to the CB near the k-valley position of Brillouin zone (BZ). Another absorption peak at around 400nm blue wavelength occurs due to the 'C' excitonic transition from VB to CB at band nesting position between Γ and Λ position of BZ [12-14]. In general electronic transitions may occur mainly in three different ways namely, (a) transition involving s, p and n electrons, (b) transition involving charge transfer and (c) transition involving d and f electrons. Both Mo (d block) and W (f block) are transition metals containing unfilled d orbitals. The transition in d-d or f-f orbitals corresponds to a UV-Vis range of light. The presence of S ligand in MoS_2 splits the d orbitals of Mo which in turn facilitate the electronic transition inside the crystal on exposure to radiation of suitable energy.

In order to determine the optical BG energy (E_g) of the as-synthesized material, we have applied the Kubelka Munk theory of diffused reflectance spectra [10]. The KM plot is similar to the Tauc Plot which is obtained from absorption spectra. The KM function F(R) is obtained using relation (3.3).

$$F(R) = \frac{(1-R)^2}{2R} \tag{3.3}$$

where R is the reflection coefficient. The optical BG energy is determined using relation (3.4).

$$F(R)E = C_3\left(E - E_g\right)^{1/m} \tag{3.4}$$

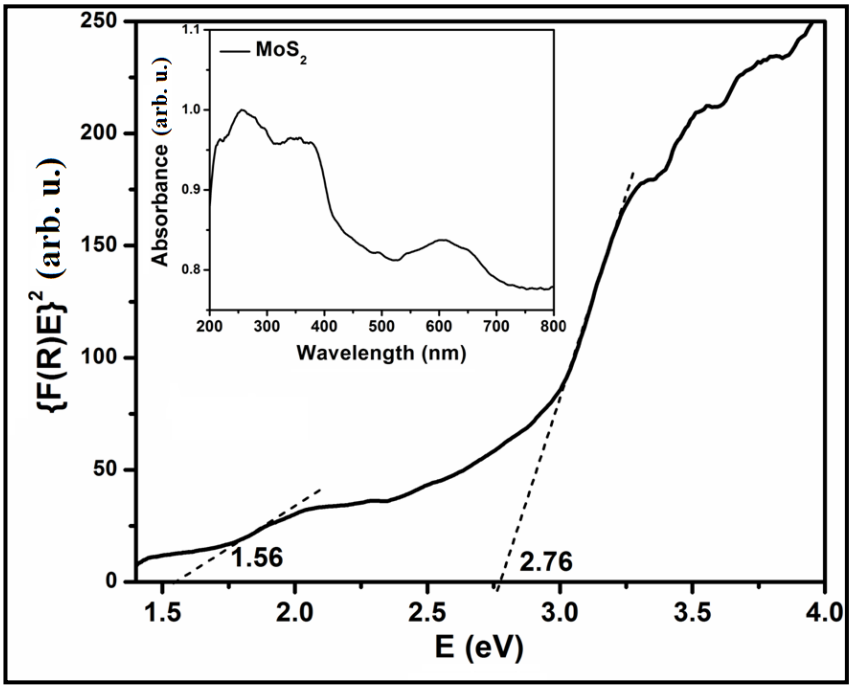

Figure 3.6 Optical BG determination by using KM plot of MoS_2 NPs (inset is UV-vis spectrum).

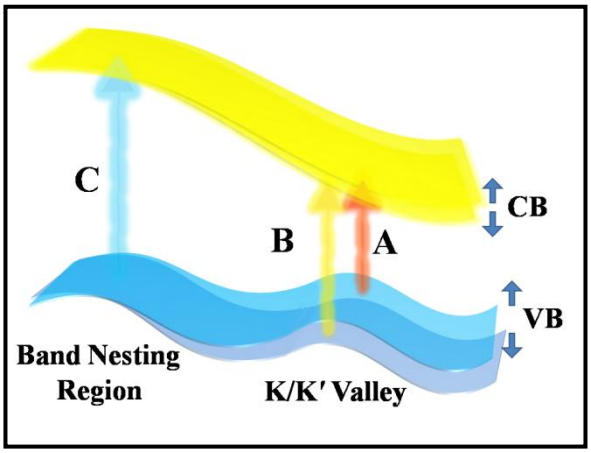

Figure 3.7 Schematic of 'A', 'B' and 'C' excitonic transition in TMDs.

where m=2, 2/3, 1/2 and 1/3 are for direct allowed transition, direct forbidden transition, indirect allowed transition and indirect forbidden transition respectively, $E = h\nu$, the energy of radiation, h and ν represents Planck's constant and frequency of vibration respectively. C_3 is the proportionality constant. The KM plot of the as-synthesized sample is shown in figure 3.6. The optical BG energy is determined by extrapolating the straight part of the KM plot as given in table 3.3.

Table 3.3 Optical energy BG calculation of MoS_2 NPs using KM plot.

Sample	**E_g (eV)**
MoS_2	2.76, 1.56

It has been observed from KM plot that the transitions for the material is multiple and hence leads to multiple band gap (MBG) material. Large values of BGs is due to the 'C' excitonic transition at band nesting position [12, 14]. In MoS_2 there are two band gap values at 1.56eV and 2.76eV. The higher value of BG energy confirms the nano scale dimension of the material system [15].

The photoluminescence property of as-synthesized MoS_2 NPs is also studied. A comparative analysis of the luminescent nature of this sample along with other prepared samples is given in section 3.4 of this chapter.

3.2 Structural and optical properties of WS_2 NPs

3.2.1 Structural characterizations of WS_2 NPs

The structural characterizations of WS_2 NPs were also carried out in a similar way like that done for MoS_2 NPs. The powder XRD pattern of this sample is shown in figure 3.8(a). The simulated PXRD plot of WS_2 is also shown in comparison with the experimental XRD plot in figure 3.8(b). In the XRD pattern of WS_2 sample the peaks at 2θ values 14.36°, 32.77°, 33.59°, 35.94°, 39.60°, 44.29°, 49.79° and 58.49° correspond to (002), (100), (101), (102), (103), (104), (105) and (110) planes respectively (JCPDS No. 84-1398). The XRD also reveals hexagonal symmetry (SG:$p6_3/mmc$) in WS_2 lattice. The average crystallite size of WS_2 NPs calculated using relation 3.1 is obtained to be approximately 13.02 nm.

TEM micrograph is also obtained for the as-synthesized WS_2 NPs and is shown in figure 3.9(a). The crystal plane spacing of 0.62nm observed in the TEM micrograph shown in figure 3.9(a) corresponds to the Millar plane (002) in the WS_2 crystal. Figure 3.9(b) shows the SAED pattern of WS_2 NP sample as obtained using TEM. The SAED rings (100), (102) and (105) correspond to characteristic crystal planes of WS_2 NPs as obtained in the respective XRD pattern.

The SEM micrograph and EDX pattern of WS_2 NPs are shown in figure 3.10(a & c). The particle size distribution of WS_2 sample is measured from SEM micrographs. From the particle size distribution histogram in figure 3.10(b) it was found that the average particle size for WS_2 sample was 50.33nm. From the EDX spectra analysis, given in figure 3.10(c), we conclude that the composition of the sample is mainly W and S, S being most abundant (table 3.4). Both XRD spectra and EDX spectra reveal the formation of WS_2.

Table 3.4 Percentage composition of WS_2 from EDX spectrum.

Element	Weight%	Atomic%
S K	30.42	71.48
W L	69.58	28.52
Total	100.00	

In the EDX spectra characteristic peak near 2.31keV confirms the presence of sulfur and near 1.8keV, 7.29keV, 8.4keV, 9.8keV and 11.25keV represents tungsten in the respective sample [5, 16]. Analyzing the elemental mapping using EDX spectroscopy the abundance of specific elements and chemical composition of the as-synthesized WS_2 NPs

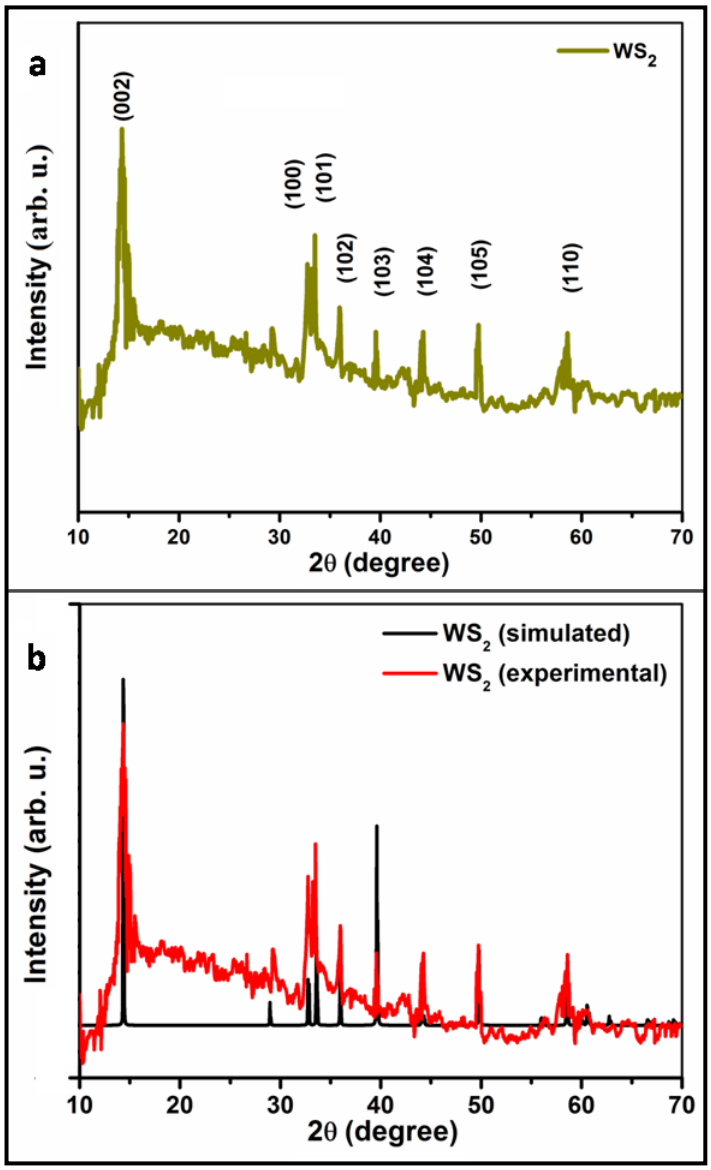

Figure 3.8 (a) XRD pattern of WS_2 NPs showing different characteristic peaks corresponding to Miller crystal planes and (b) Comparison of XRD pattern of WS_2 with simulated PXRD of WS_2.

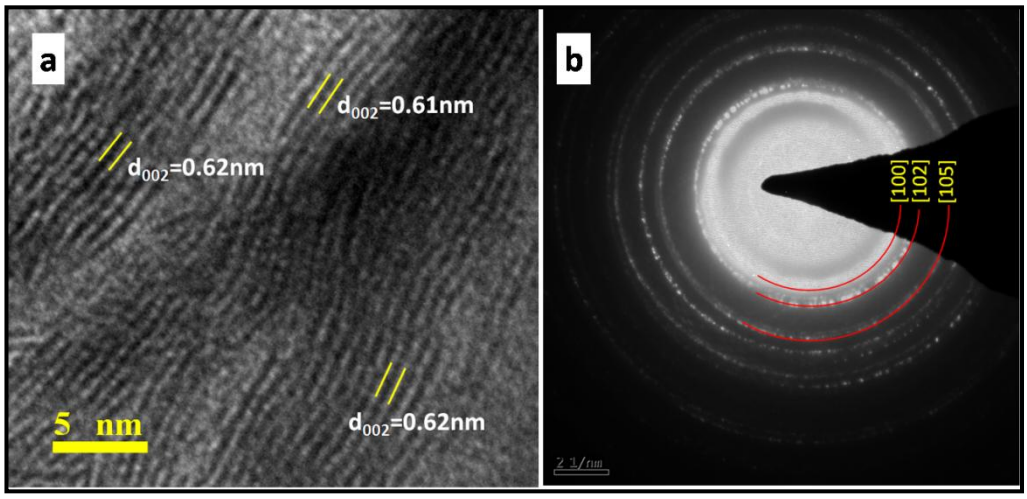

Figure 3.9 (a) TEM micrograph and (b) SAED pattern of WS_2 NPs sample.

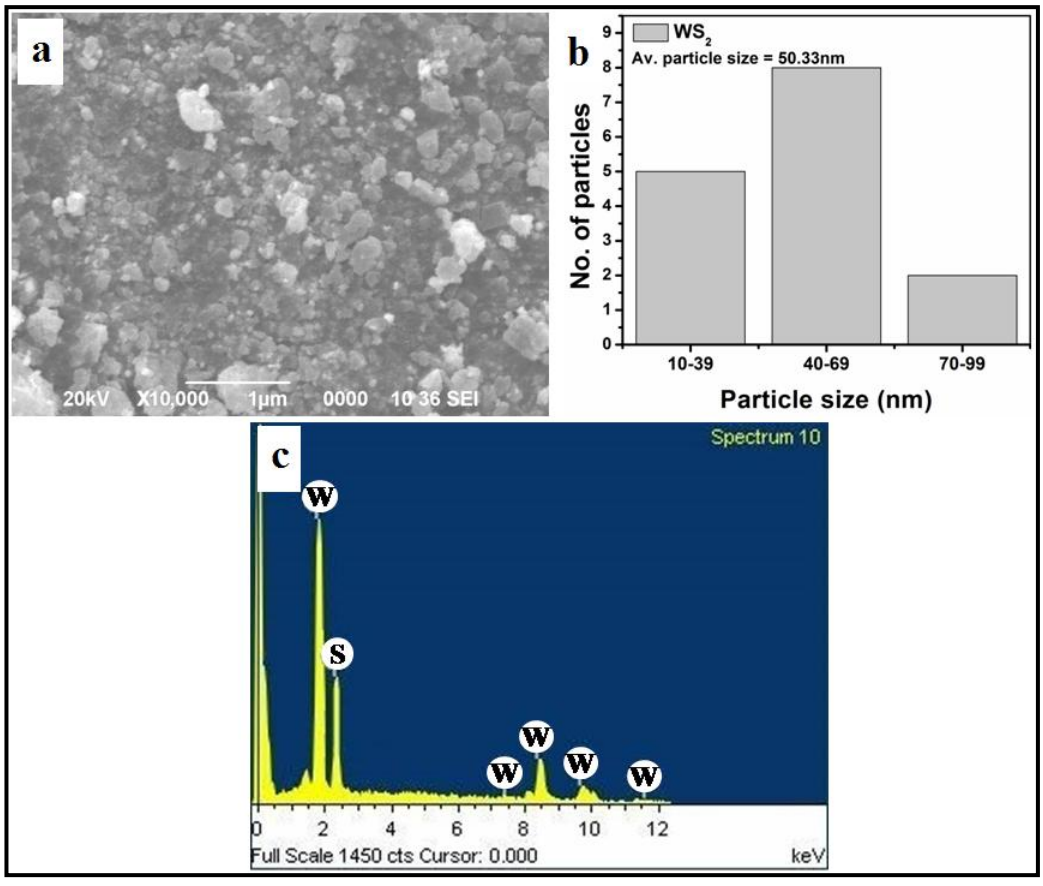

Figure 3.10 (a) SEM image, (b) particle size distribution and (c) EDX spectrum of WS_2 NPs sample. The noise peak observed below 0.5keV is not taken into consideration.

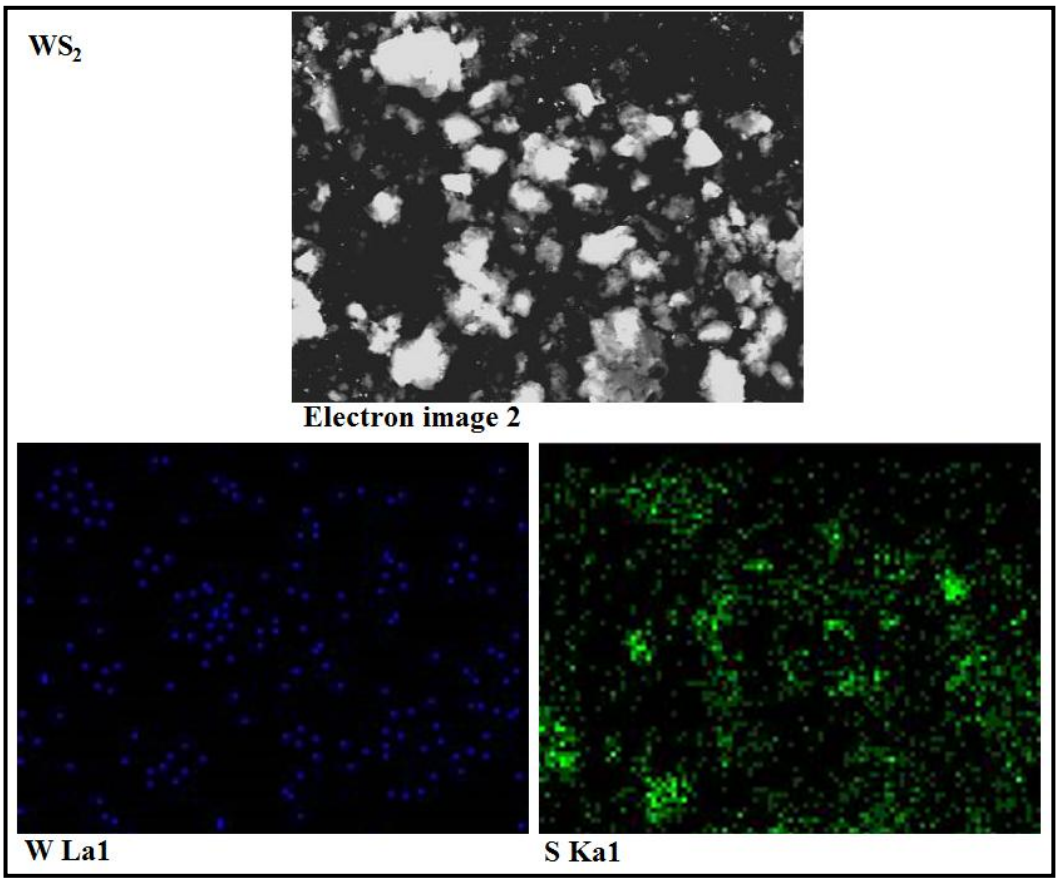

Figure 3.11 EDX elemental mapping of WS_2 NPs sample. The bright spots in a black background in the second and third image represent the positions of respective elements W and S in the selected area.

are clearly visualized as given in figure 3.11.

In figure 3.12 the Raman spectrum of WS_2 NPs is shown. The characteristic peaks 348.34cm^{-1} and 420.01cm^{-1} in the Raman spectrum of WS_2 NPs sample reveal the Raman active vibrational mode E^1_{2g} and A_{1g} in WS_2. There is also shift in the two prominent modes in the WS_2 NPs sample from that of bulk structure, which may be due to the similar effect like that for MoS_2 sample as described in section 3.1.1[7, 8]. The resonance mode $A_{1g} + LA(M)$ at 593.07cm^{-1} which may occur due to comparable excitation energy with BG value of the material is also recognizable. The phonon lifetime is calculated from the Raman active mode peaks and is tabulated in table 3.5. Here also the phonon lifetimes corresponding to the prominent Raman active modes E^1_{2g} and A_{1g} are found to be in picosecond range like that of MoS_2 NP sample indicating defective traps in the NPs.

Table 3.5 Determination of phonon lifetime in WS_2 NPs sample from Raman spectrum.

Peak position (cm^{-1})	**Phonon Lifetime (ps)**
348.34	1.67
420.01	1.96

3.2.2 Optical characterizations of WS_2 NPs

The UV-Vis spectrum of the WS_2 NP sample is shown in the inset of figure 3.13. The spectrum shows good absorption of light in the visible region as well as in the UV region. The KM plot of the WS_2 NPs sample is shown in figure 3.13. The optical BG (Eg) energy is determined from the KM plot and tabulated in table 3.6. Like MoS_2 NPs sample, we have also observed two BG values which are probably due to a different phase or dimensional effect [17, 18].

Table 3.6 Optical Energy BG calculation of WS_2 NPs using KM plot.

Sample	**E_g (eV)**
WS_2	2.74, 1.58

The PL property of the as-synthesized WS_2 NP is also studied. A comparative analysis of the luminescence property of this sample along with other prepared samples is given in section 3.4 of this chapter.

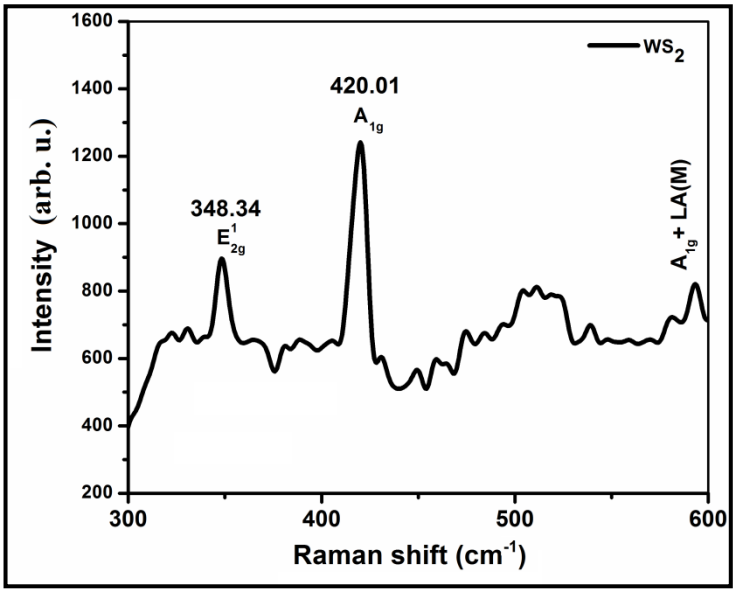

Figure 3.12 Raman spectrum of WS_2 NPs showing prominent Raman active modes in the sample.

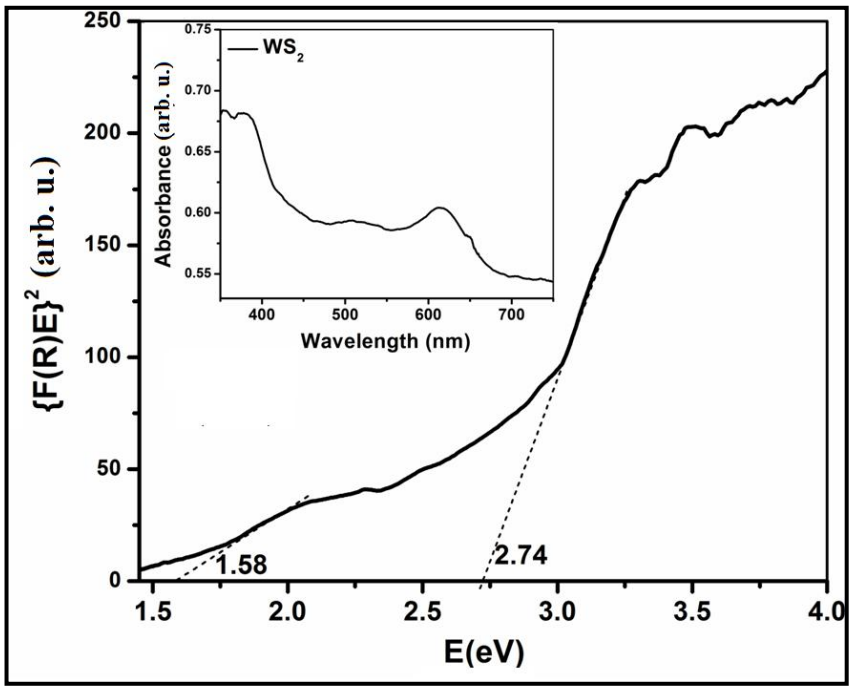

Figure 3.13 Optical BG determination by using KM plot of WS_2 NPs (inset is UV-vis spectrum).

3.3 Structural and optical properties of ternary MoW-disulfide compound NPs

3.3.1 Structural characterizations of ternary MoW-disulfide compound NPs

The plots of figure 3.14 show the XRD patterns for the four prepared sample materials namely MoS_2, WS_2, MoW-disulfied1 and MoW-disulfide2 NPs. The different crystal planes in the XRD plot (iii) and plot (iv) in figure 3.14 revealed the crystallinity of the as-prepared compound materials. In plot (i) and plot (ii) of figure 3.14, the prominent characteristic peaks and various crystal planes of MoS_2 and WS_2 NPs are revealed. The XRD patterns as shown by the plot (iii) and plot (iv) of the MoW-disulfide1 and MoW-disulfide2 samples are quite different from that of MoS_2 and WS_2 NPs. This outcome indicated the possible formation of new bonding structures between Mo, W and S. This result provides us information about the formation of a ternary disulfide compound of Mo and W. In comparison with MoS_2 and WS_2 structures, the different possible crystal plane positions were obtained in the respective XRD plots of the compounds. The possible Miller planes corresponding to respective 2θ values and d-spacing values for ternary compounds are tabulated in table 3.7 and table 3.8. The d spacing values are obtained using Bragg's law of diffraction in crystal planes and are given by formula 3.5.

$$d_{hkl} = \frac{m\lambda}{2Sin\theta} \tag{3.5}$$

where d_{hkl} is the spacing between consecutive crystal planes, λ and θ are the wavelength of X-ray used and Bragg's angle respectively, m is the order of diffraction which is equal to one in our current study.

Table 3.7 2θ, Millar planes and d-spacing values for MoW-disulfide1 NPs.

2θ (degree)	23.12	28.75	33.17	34.17	35.49	44.57	49.76	59.84
d-spacing (Å)	3.85	3.10	2.69	2.62	2.53	2.03	1.83	1.54
Miller Plane	(003)	(004)	(100)	(101)	(102)	(006)	(105)	(008)

The average crystallite sizes (L) of MoW-disulfide1 and MoW-disulfide2 are calculated using the Debye-Scherrer formula 3.1 and found to be 22.02nm and 18.30nm respectively. The increase in crystallite size in the as-synthesized compound

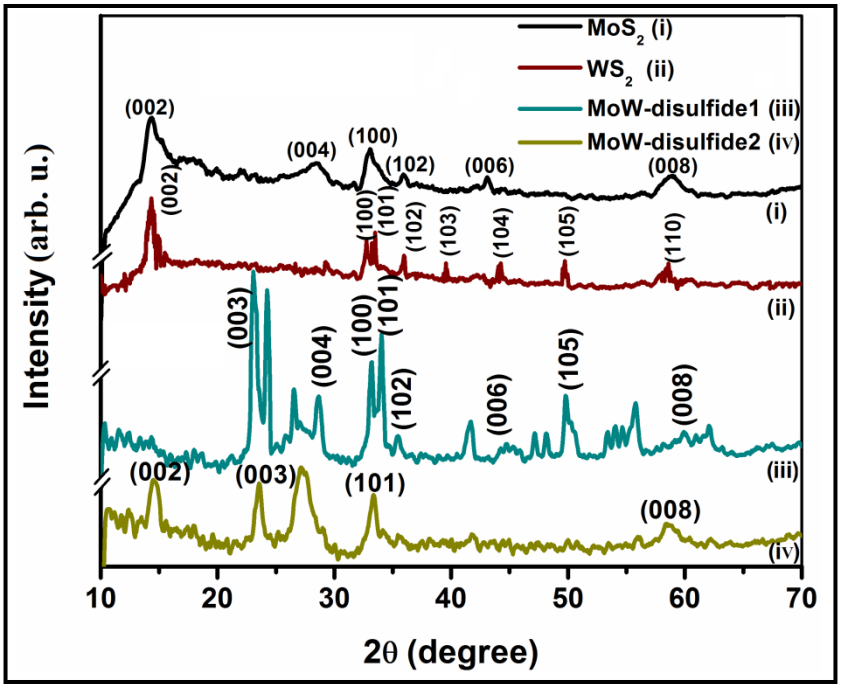

Figure 3.14 XRD patterns of (i) MoS_2, (ii) WS_2, (iii) MoW-disulfide1 and (iv) MoW-disulfide2 NPs sample.

Table 3.8 2θ, Miller planes and d-spacing values for MoW-disulfide2 NPs.

2θ (degree)	14.52	23.53	33.41	59.01
d-spacing (Å)	6.10	3.78	2.68	1.56
Miller Plane	(002)	(003)	(101)	(008)

MoW-disulfide1 relative to MoS_2 and WS_2 reflects that W forms a better crystal with S compared to Mo. In MoW-disulfide2 the crystallite size again decreases as the concentration of W compared to Mo decreases. Therefore, it reaffirms the fact that the combination of W and S leads to better crystallinity than the combination of Mo and S.

The TEM micrographs of the compound MoW-disulfide1and MoW-disulfide2 NPs are also analyzed to study the crystal planes present in the as-prepared samples. Figure 3.15 shows the TEM images where different possible Millar planes are indicated in the compound NPs. TEM analysis confirms that the NPs are polycrystalline in nature. The interplannar spacings 0.31nm and 0.39nm measured from in the TEM micrograph 3.15(a) are possibly be due to (004) and (003) Millar planes respectively in MoW-disulfide1 NPs and spacings 0.63nm and 0.40nm in figure 3.15(b) represent Miller planes (002) and (003) respectively in MoW-disulfide2 NPs considering the structure of the ternary compound to be hexagonal, the most stable structure in case of TMDs. The results of XRD and TEM, both reveal that the possible crystal structure of the compound NP is hexagonal like that of MoS_2 and WS_2.

The SEM micrographs along with the particle size distribution of the as-synthesized ternary compound materials are shown in figure 3.16. The average particle sizes for MoW-disulfide1 and MoW-disulfide2 NPs are found to be 51.40nm and 57.26nm respectively (figure 3.16(b & e). The agglomeration of particles is also visible in the SEM micrographs.

From the EDX spectra, given in figure 3.16(c & f), we conclude that MoW-disulfide1 and MoW-disulfide2 are mainly composed of Mo, W and S, S being most abundant. The abundance of W in MoW-disulfide1 is richer than that of MoW-disulfide2. Both XRD spectra and EDX spectra reveal the formation of ternary MoW-disulfides compound.

In the EDX spectra in figure 3.16(c & f) characteristic peaks at 2.31keV confirm the presence of sulfur; at 2.39keV reveal the presence of molybdenum and near 1.8keV, 7.29keV, 8.4keV, 9.8keV and 11.25keV represent the presence of tungsten in the

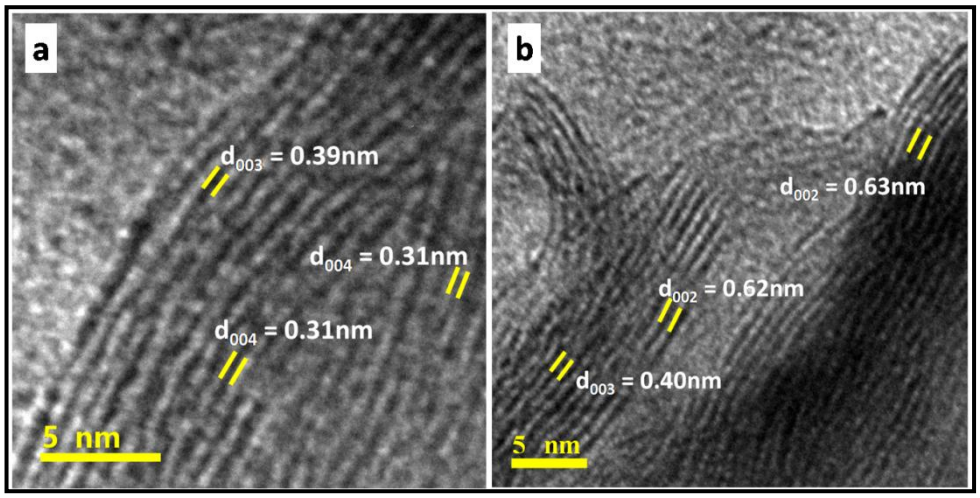

Figure 3.15 TEM micrograph of (a) MoW-disulfide1 and (b) MoW-disulfide2 showing different Miller planes.

respective samples. From the EDX spectrographs of the compound materials, the weight% and atomic% along with the characteristic transition levels are tabulated in table 3.9 and table 3.10. From table 3.9 and table 3.10, it is found that in MoW-disulfide1 the main

Table 3.9 Percentage composition of MoW-disulfide1 from EDX spectrum.

Element	Weight%	Atomic%
S K	23.25	60.36
Mo L	11.79	10.23
W M	64.96	29.41
Total	100.00	

Table 3.10 Percentage composition of MoW-disulfide2 from EDX spectrum.

Element	Weight%	Atomic%
S K	63.34	86.23
Mo L	23.31	10.60
W M	13.35	3.17
Total	100.00	

elements present are Mo, W and S with Mo:W atomic % ratio 1:3, and in MoW-disulfide2 Mo:W atomic % ratio 3:1, S being most abundant in both MoW-disulfide1 and MoW-disulfide2. Also, the presence of the characteristic peaks of Mo, W and S in EDX spectra confirms their existence in the respective materials. The abundance of specific elements and chemical composition of the as-synthesized ternary compounds are envisioned in the elemental maps or spot chemical analysis using EDX spectroscopy given in figure 3.17 and figure 3.18. The bright spots in the mapped images represent the corresponding element which could be visualized due to the characteristic transition Ka1 for S, La1 for Mo and La1 for W atoms [5, 16].

Raman spectra of the compounds MoW-disulfide1 and MoW-disulfide2 were also obtained and are shown in figure 3.19. The Raman spectra of these materials were obtained at laser excitation wavelength of 488nm (2.54eV) as obtained in the case of MoS_2 and WS_2 NPs. The characteristic peaks obtained in case of MoS_2 are also observed in the Raman spectrum (figure 3.19(b)) of MoW-disulfide2 having smaller W content with slight shift in peaks which is due to the dominant effect of larger Mo content; but in case of MoW-disulfide1 having larger W content, no significant results could be drawn in the absence of recognizable peaks (figure 3.19(a)). However the formation of new bonds cannot be ruled

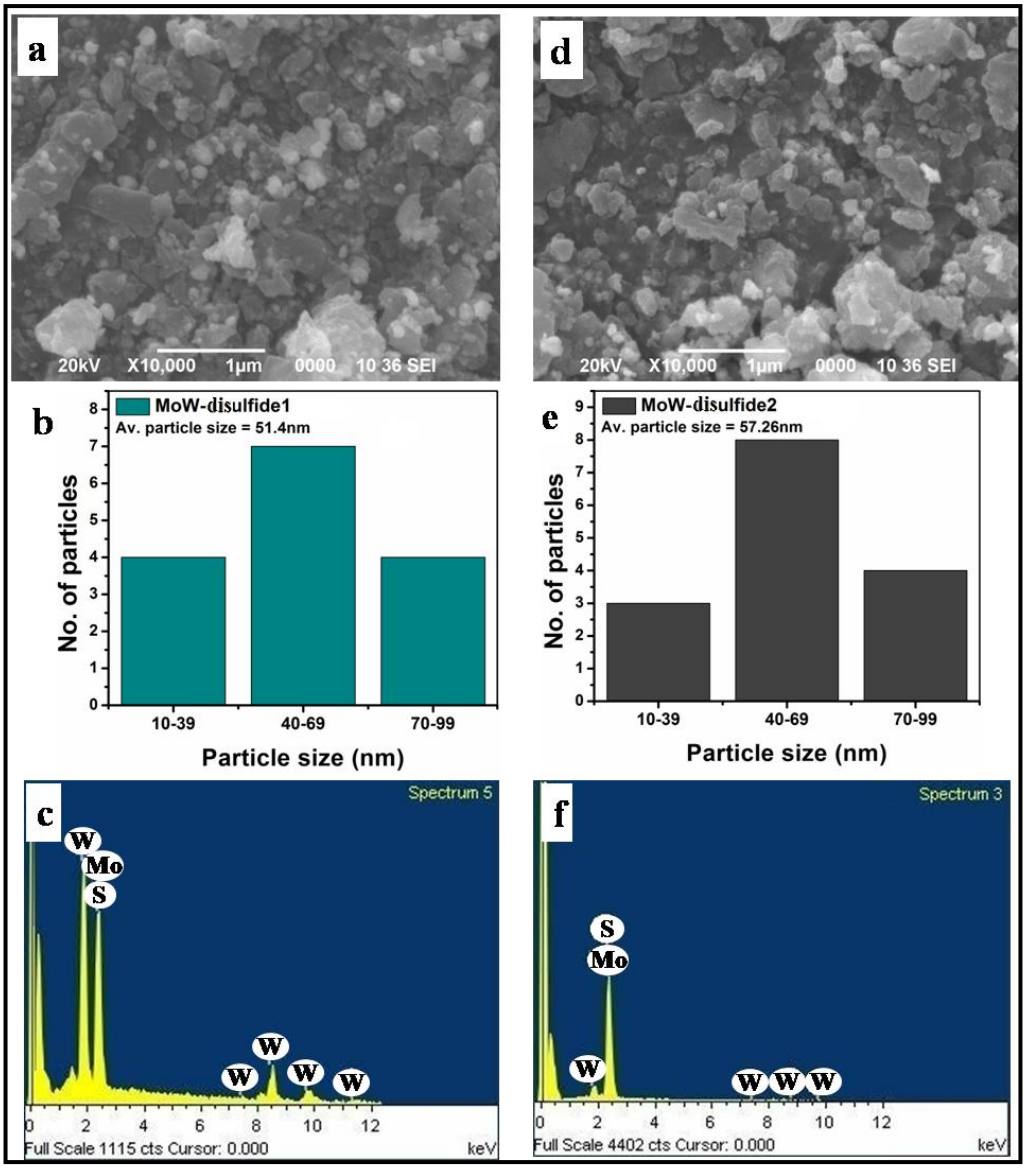

Figure 3.16 Figure shows (a) SEM image, (b) particle size distribution and (c) EDX spectrum of MoW-disulfide1 NPs and (d) SEM image, (e) particle size distribution and (f) EDX spectrum of MoW-disulfide2 NPs.

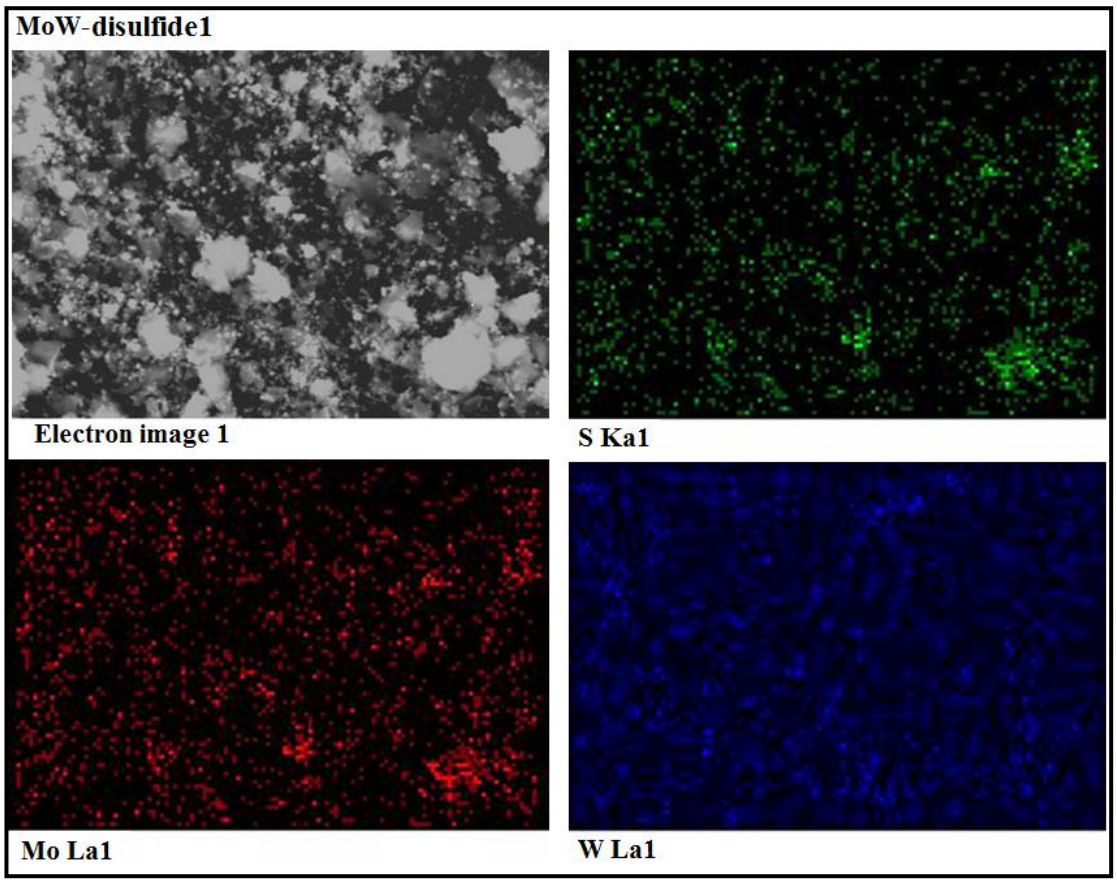

Figure 3.17 EDX Elemental mapping of MoW-disulfide1. The bright spots in black background in the second, third and fourth images represent the positions of respective elements S, Mo and W in the selected area.

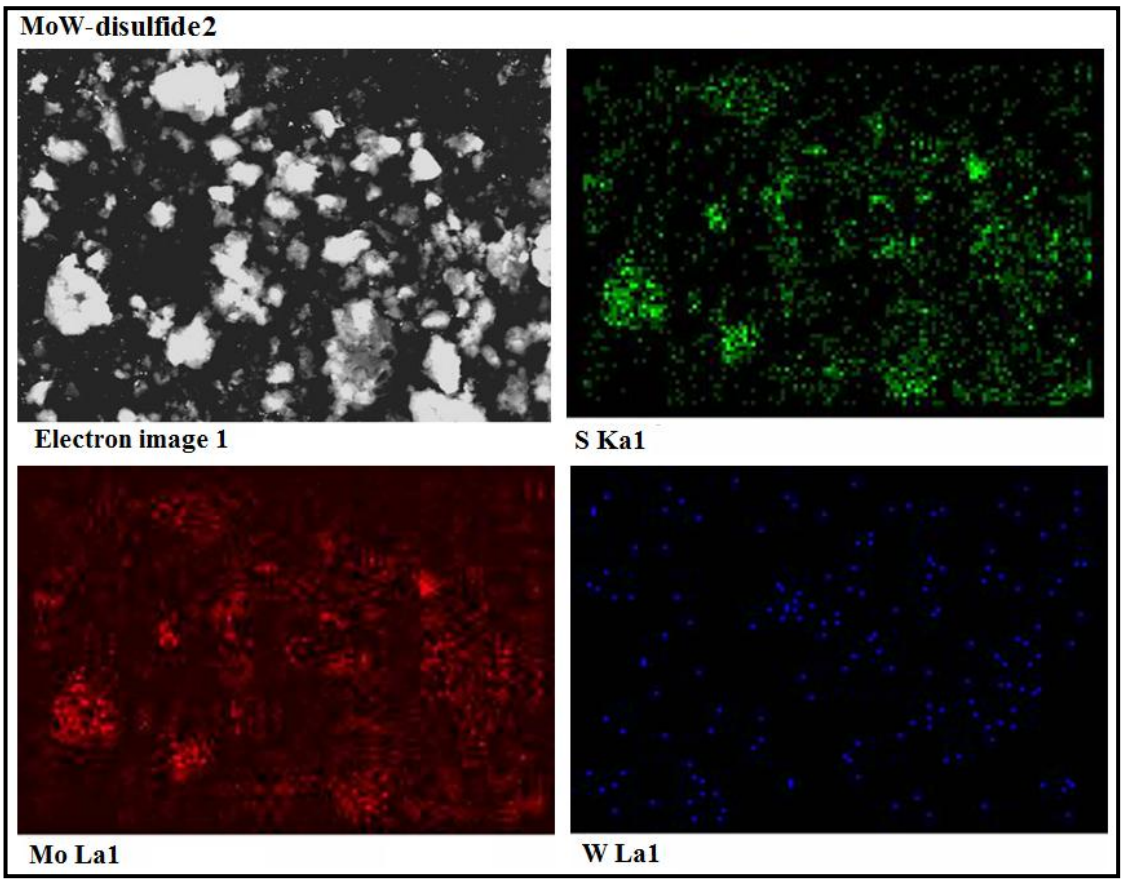

Figure 3.18 EDX Elemental mapping of MoW-disulfide2. The bright spots in black background in the second, third and fourth images represent the positions of respective elements S, Mo and W in the selected area.

out. The phonon lifetimes of the ternary dichalcogenide NPs corresponding to prominent Raman peaks are calculated using the energy-time uncertainty relation 3.2 and are tabulated in table 3.11. Large values of phonon lifetime in the picosecond range depict the stability of phonons in the defects of the ternary compound NPs.

Table 3.11 Determination of phonon lifetime in MoW-disulfide1 and MoW-disulfide2 samples from the Raman spectra.

Sample	**Peaks(cm^{-1})**	**Phonon lifetime (ps)**
MoW-disulfide1	329.96	2.39
MoW-disulfide2	382.08	2.49
	404.57	2.34

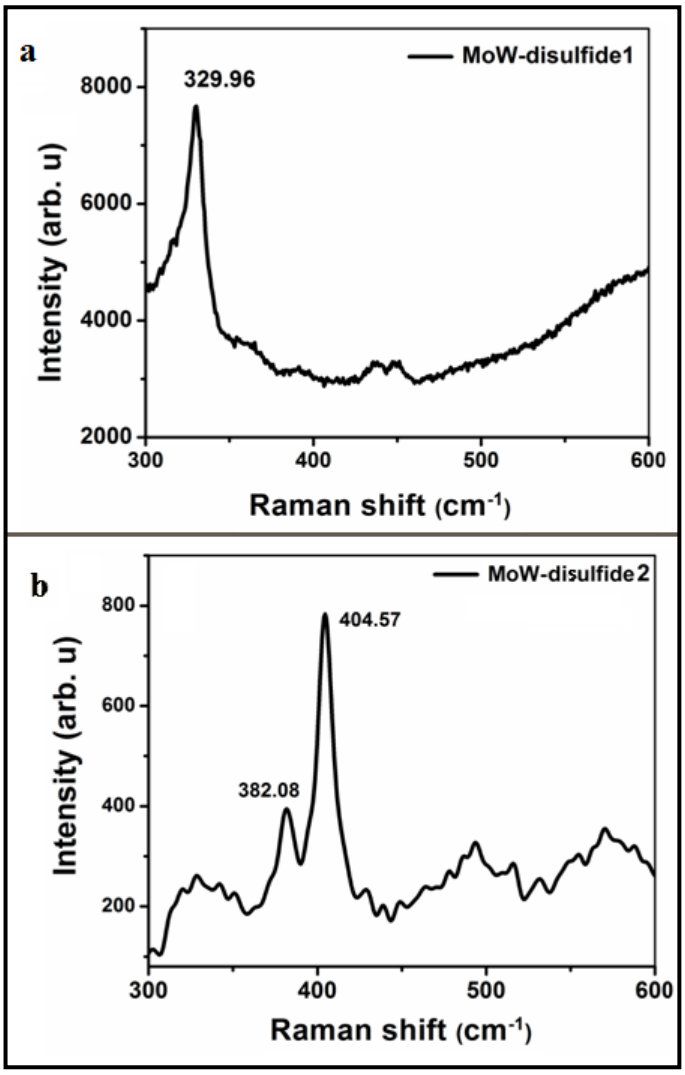

Figure 3.19 Raman spectra of (a) MoW-disulfide1 NPs and (b) MoW-disulfide2 NPs.

3.3.2 Optical characterizations of ternary MoW-disulfide compound NPs

In figure 3.20 we show the KM plots obtained from UV-vis spectra of the two as-synthesized compound materials namely MoW-disulfide1 and MoW-disulfide2 NPs. The inset of figure 3.20 shows the UV-vis spectra of the two compounds. The nature of absorption of light of these prepared compound NPs is not different from that of MoS_2 and WS_2 NPs. The absorption spectra reveal good absorption of light in both UV and visible wavelengths by the two compounds. From the KM plot, the optical BG energy values are determined for the two compounds and given in the table 3.12. KM plot indicates the existence of multiple transitions in the NP materials and hence allows MBG values. Due to transition at band nesting position there exist high values of optical BGs in the compound materials [12-14]. In MoW-disulfide2, there are two band gap values whereas in MoW-disulfide1 there are possibly three BG values. The dominance of W in MoW-disulfide1 may be the reason behind having an extra band gap value compared to the other compound sample.

Table 3.12 Optical Energy BG calculation of MoW-disulfide1 and MoW-disulfide2 using KM plot.

Sample	**E_g (eV)**
MoW-disulfide1	2.84, 2.41, 1.65
MoW-disulfide2	2.65, 1.45

From table 3.12 it is found that the compound ternary disulfide1 have the highest BG energy which corresponds to visible blue light wavelength. The increase in BG for this sample is due to the insertion of a bigger atom like W in the lattice site of MoS_2. Actually, the above anomalies in MoW-disulfide1 may be due to the combined effect of ligand S and W which leads to spin splitted d-orbitals that raise the energy levels and provides an extra energy gap value as well. This, in turn, increases the BGs. As the size of the material reduces, the number of overlapping orbitals or energy levels (both bonding and antibonding orbitals) decreases. This results in narrower bands and the band gap increases. The high BG energy of the ternary compound samples confirms the nanoscale dimension of the material system [15].

The PL behavior of the as-synthesized ternary compound NPs is given in the following section 3.4 and compared with MoS_2 and WS_2 NP samples.

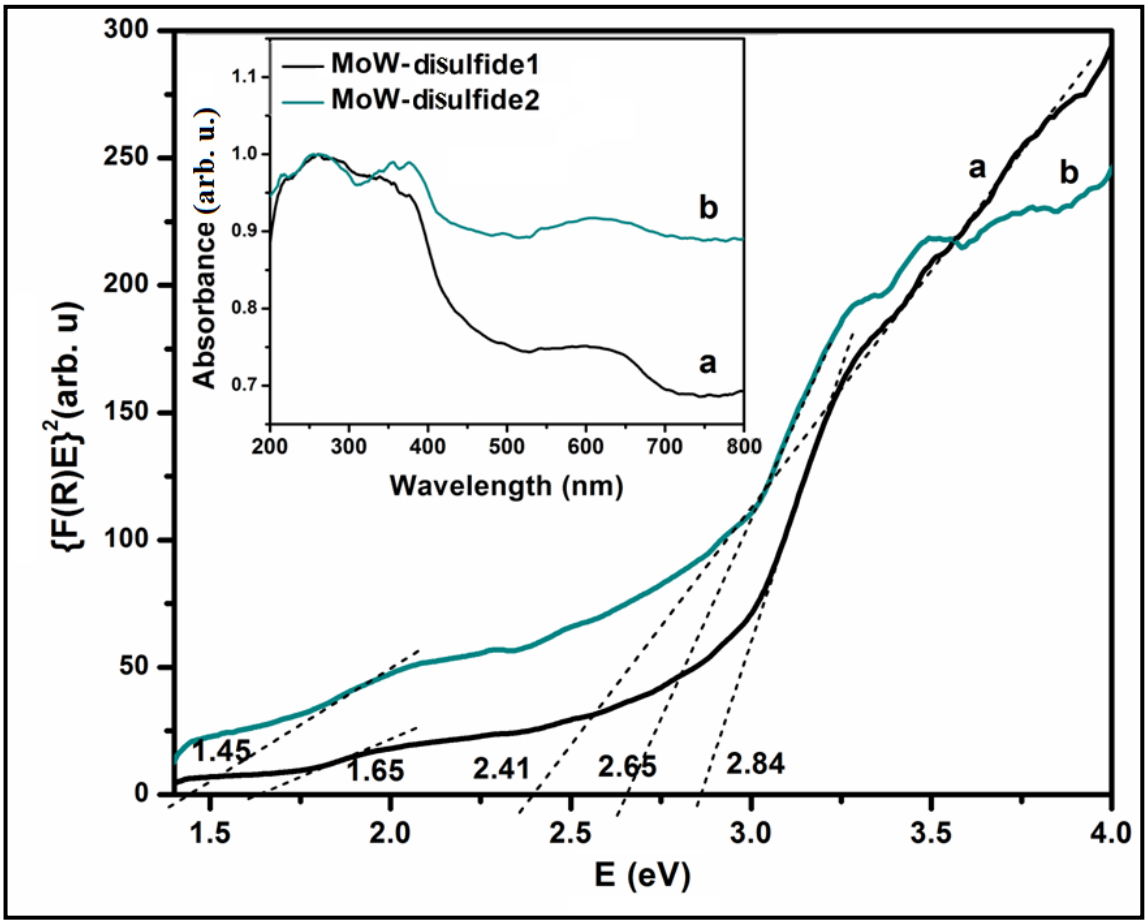

Figure 3.20 Optical BG determination by using KM plot of compound (a) MoW-disulfide1 and (b) MoW-disulfide2 NPs (inset is UV-vis spectra).

3.4 Study of photoluminescence spectra of MoS_2, WS_2, MoW-disulfide1, and MoW-disulfide2 NPs

Being SCs, PL is investigated in our as-synthesized materials. The PL spectra of the as-synthesized materials are shown in figure 3.21. We have analyzed the PL spectra to measure the emission BG of new compound SC NPs as well as MoS_2 and WS_2 NPs. The chosen excitation wavelengths are in the UV (300nm) region in plot 3.21(a) and Visible (500nm) region in plot 3.21(b).

Analyzing the PL spectra in figure 3.21, it has been observed that there is an enhancement in the luminescence of the compound disulfide having larger W:Mo ratio. The luminescence peaks are observed at approx. 659nm (1.88eV) for excitation wavelength of 500nm and at approx. 462nm (2.68eV) for excitation wavelength of 300nm. In case of MoW-disulfide1 NPs, the PL peak is enhanced by about two times compared to that of MoS_2 NPs and 1.7 times than that of WS_2 NPs. It is observed that WS_2 NPs have slightly higher PL intensity than that of MoS_2 NPs. This may be due to the effect of a larger W atom which provides more exciton pairs compared to MoS_2 NPs. The compound disulfides of W and Mo combination having larger W content give rise to an increase in luminescence. Larger W content in the ternary compound enhances the PL intensity. This is probably due to the increase in the number of photo-excitons with the insertion of W in a large amount and as a consequence higher density of generated photo-excitons increases the PL intensity by the process of radiative recombination. It can also be due to the presence of less number of defects in compound disulfide1 as it has the highest value of crystallite size [20]. The near BG emission in the PL spectra also reveals the possibility of direct BG nature of the as-synthesized dichalcogenides and the PL can be considered to be band edge emission. We have also investigated the effect of W and Mo in their ternary compound theoretically using DFT based software. DFT investigation (discussed in chapter 5) reveals that W insertion in the MoS_2 system leads the system towards becoming direct BG SC which, in turn, may lead to enhanced PL emission as observed in our experiment. In figure 3.22 a schematic of photoexcitation and radiative recombination of exciton pairs is described.

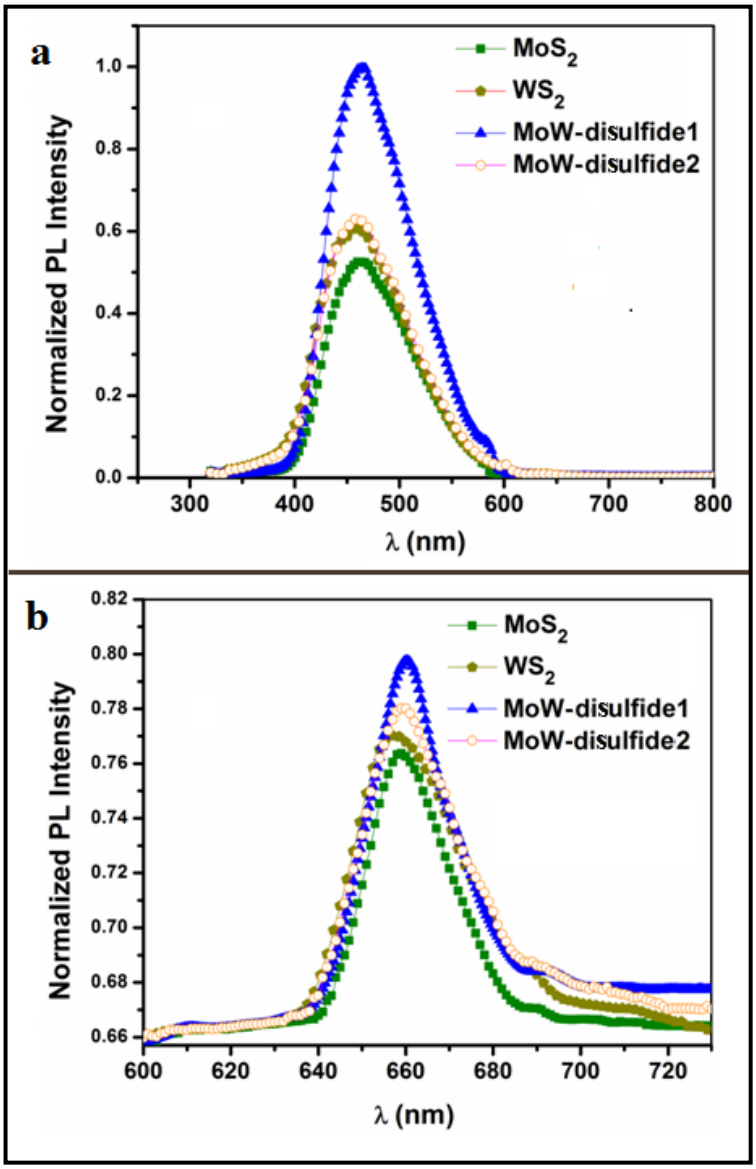

Figure 3.21 PL spectra of MoS_2, WS_2, MoW-disulfide1 and MoW-disulfide2 at (a) 300nm (4.13eV) and (b) 500nm (2.48eV). The enhancement of PL peak is observed in case of ternary compound MoW-disulfide1 having largest normalized intensity.

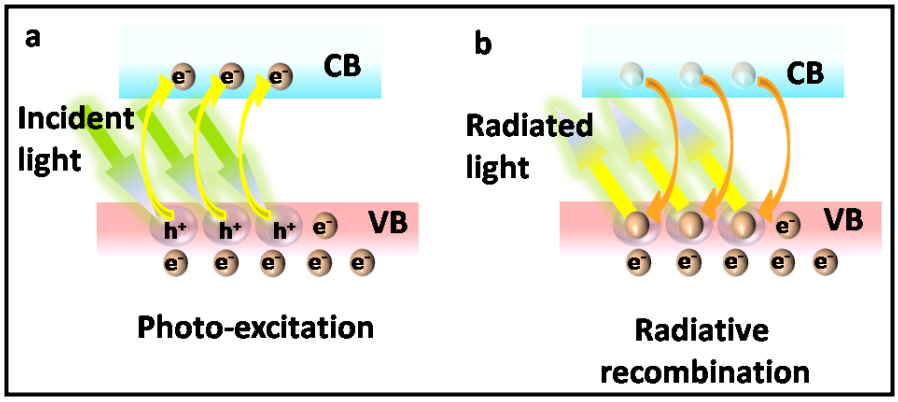

Figure 3.22 The figure shows (a) the excitation of a direct BG semiconductor by light radiation generating electron-hole pairs and (b) re-emission of light by the process of radiative recombination of electron and holes.

3.5 Conclusions

In this chapter we have reported the structural properties, optical emission properties and chemical composition of the as-synthesized SC TMDs compound NPs along with MoS_2 and WS_2 NPs. XRD, SEM, TEM, EDX and Raman spectra analyses reveal the formation of desired materials having nanoscale size distributions. It has been observed from UV-Vis and PL spectra that the combining effect of the sulfides of W and Mo gives rise to different optical properties. Enhanced blue PL emission near 463nm in MoW-disulfide1, having Mo:W molar ratio equal to one, indicates the material's good applicability in luminescence devices. Also, multiple band gaps of the ternary compound promise the material to be a good material for photocatalytic activity.

[Note: This work is published in the Journal Bulletin of Materials Science.

Kalita, D., Chetia, L. Chetri, P., and Ahmed, G. A. Investigation of structural and luminescence properties of nanocrystalline Tungsten incorporated Molybdenum disulfide ternary compounds: An Experimental and DFT Study. *Bull. Mater. Sci.*, 42:134, 2019. DOI: 10.1007/s12034-019-1796-2]

References

[1] Chetia, L., Kalita, D., Ahmed, G. A. Enhanced photocatalytic degradation by diatom templated mixed phase titania nanostructure. *Journal of Photochemistry and Photobiology A: Chemistry*, 338:134-145, 2017. DOI: 10.1016/j.jphotochem.2017.01.035

[2] Momma, K., and Izumi, F. VESTA 3 for three-dimensional visualization of crystal, volumetric and morphology data. *J. Appl. Cryst.* 44:1272-1276, 2011. DOI:10.1107/S0021889811038970

[3] Krinke, T., Deppert, K., Magnusson, M., Fissan, H., and Schmidt, F. Agglomeration of nanoparticles on substrate surfaces due to particle interactions during deposition. *J. Aerosol Sci.*, 29:S1281-S1282, 1998.

[4] Bantz, C., Koshkina, O., Lang, T., Galla, H.-J., C. Kirkpatrick, J., Stauber, R. H. and Maskos, M. The surface properties of nanoparticles determine the agglomeration state and the size of the particles under physiological conditions. *Beilstein J. Nanotechnol.*, 5:1774-1786. 2014. DOI:10.3762/bjnano.5.188

[5] Angeles-Chavez, C., Toledo-Antonio, J. A. and Cortes-Jacome, M. A. Chemical Quantification of Mo-S, W-Si and Ti-V by Energy Dispersive X-Ray Spectroscopy. In Dr. Shatendra K Sharma, editor, *X-Ray Spectroscopy*, pages 119-13., ISBN: 978-953-307-967-7, InTech, 2012. Available from: http://www.intechopen.com/books/x-ray-spectroscopy/chemical-quantification-of-mo-s-w-si-and-ti-v-by-energydispersive-x-ray-spectroscopy

[6] Frey, G. L. and Tenne, R. Raman and resonance Raman investigation of MoS_2 nanoparticles. *PHYSICAL REVIEW B*, 60(4):2883-2892, 1999.

[7] Zhang, X., Han, W. P., Wu, J. B., Milana, S., Lu, Y., Li, Q. Q., Ferrari, A. C., and Tan, P. H. Raman spectroscopy of shear and layer breathing modes in multilayer MoS_2. *PHYSICAL REVIEW B*, 87:115413, 2013. DOI: 10.1103/PhysRevB.87.115413

[8] Li, H., Zhang, Q., Yap C. C. R., Tay, B. K., Edwin, T. H. T., Olivier, A., and Baillargeat, D. From Bulk to Monolayer MoS_2: Evolution of Raman Scattering. *Adv. Funct. Mater.*, 22:1385-1390, 2012. DOI: 10.1002/adfm.201102111

[9] Estreicher, S. K., Gibbons, T. M., Bebek, M. B., Cardona, A. L. Heat flow and defects in semiconductors: beyond the phonon scattering assumption. *Solid State Phenomena*, 242:335-343, 2016.

[10] Makama, A. B., Salmiaton, A., Saion, E. B., Choong, T. S. Y., and Abdullah, N. Synthesis of CdS Sensitized TiO2 Photocatalysts: Methylene Blue Adsorption and Enhanced Photocatalytic Activities. *International Journal of Photoenergy*, 2016:1-14, 2016. DOI:10.1155/2016/2947510

[11] Kalita, D., Chetia, L., Ahmed, G. A. Synthesis of MoW-Sulfide compound nanoparticles as a photocatalyst and comparison of its performance with MoS2 and WS2 nanoparticles. *Journal of Environmental Chemical Engineering*, 5:3161-3171, 2017. DOI:10.1016/j.jece.2017.06.020

[12] Kumar, R., Verzhbitskiy, I., and Eda, G. Strong Optical Absorption and Photocarrier Relaxation in 2-D Semiconductors. *IEEE JOURNAL OF QUANTUM ELECTRONICS*, 51(10), 2015. DOI: 10.1109/JQE.2015.2470549

[13] Carvalho, A., Ribeiro, R. M., and Castro Neto, A. H. Band nesting and the optical response of two-dimensional semiconducting transition metal dichalcogenides. *PHYSICAL REVIEW B*, 88:115205, 2013. DOI:10.1103/PhysRevB.88.115205

[14] Zhao, W., Ribeiro, R. M., and Eda, G. Electronic Structure and Optical Signatures of Semiconducting Transition Metal Dichalcogenide Nanosheets. *Acc. Chem. Res*., 48:91-99, 2015. DOI: 10.1021/ar500303m

[15] Frasco, M. F. and Chaniotakis, N. Semiconductor Quantum Dots in Chemical Sensors and Biosensors. *Sensors*, 9:7266-7286, 2009. DOI:10.3390/s90907266

[16] Pourabbas, B., Jamshidi, B. Preparation of MoS2 nanoparticles by a modified hydrothermal method and the photo-catalytic activity of MoS2/TiO2 hybrids in photo-oxidation of phenol. *Chemical Engineering Journal*, 138:55-62, 2008. DOI:10.1016/j.cej.2007.05.028

[17] Kang, J., Zhang, L., and Wei, S.-H. A Unified Understanding of the Thickness-Dependent Bandgap Transition in Hexagonal Two-Dimensional Semiconductors. *J. Phys. Chem. Lett.*, 7:597-602, 2016. DOI: 10.1021/acs.jpclett.5b02687

[18] Jin, W., Yeh, P. C., Zaki, N., Zhang, D., Sadowski, J. T., Al-Mahboob, A., Zande, A. M. v. d., Chenet, D. A., Dadap, J. I., Herman, I. P. Sutter, P., Hone, J., and Osgood R. M. Direct Measurement of the Thickness-Dependent Electronic Band Structure of MoS2 Using Angle-Resolved Photoemission Spectroscopy. Jr. *Phys. Rev. Lett.*, 111:106801, 2013. DOI:10.1103/PhysRevLett.111.106801

[19] Vatankhah, C. and Ebadi, A. Quantum Size Effects on Effective Mass and Band gap of Semiconductor Quantum Dots. *Res.J.Recent Sci.* 2(1):21-24, 2013.

[20] T. H. Gfroerer, Photoluminescence in Analysis of Surfaces and Interfaces, R.A. Meyers (Ed.). In *Encyclopedia of Analytical Chemistry*, pages 9209-9231, John Wiley & Sons Ltd, Chichester, 2000.